Monthly Notices
of the
ROYAL ASTRONOMICAL SOCIETY

MNRAS **452,** 431–443 (2015) doi:10.1093/mnras/stv1304

Electron and ion acceleration in relativistic shocks with applications to GRB afterglows

Donald C. Warren,[1⋆] Donald C. Ellison,[2⋆] Andrei M. Bykov[3,4,5⋆] and Shiu-Hang Lee[6]

[1]*Astrophysical Big Bang Laboratory, RIKEN, Saitama 351-0198, Japan*
[2]*Physics Department, North Carolina State University, Box 8202, Raleigh, NC 27695, USA*
[3]*Ioffe Institute for Physics and Technology, 194021 St. Petersburg, Russia*
[4]*International Space Science Institute (ISSI), Hallerstrasse 6, CH-3012 Bern, Switzerland*
[5]*St.Petersburg Polytechnic University, St. Petersburg, Russia*
[6]*Japan Aerospace Exploration Agency (JAXA), Institute of Space and Astronautical Science, Kanagawa 252-5210, Japan*

Accepted 2015 June 9. Received 2015 May 28; in original form 2015 March 20

ABSTRACT

We have modelled the simultaneous first-order *Fermi* shock acceleration of protons, electrons, and helium nuclei by relativistic shocks. By parametrizing the particle diffusion, our steady-state Monte Carlo simulation allows us to follow particles from particle injection at non-relativistic thermal energies to above PeV energies, including the non-linear smoothing of the shock structure due to cosmic ray (CR) backpressure. We observe the mass-to-charge (A/Z) enhancement effect believed to occur in efficient *Fermi* acceleration in non-relativistic shocks and we parametrize the transfer of ion energy to electrons seen in particle-in-cell (PIC) simulations. For a given set of environmental and model parameters, the Monte Carlo simulation determines the absolute normalization of the particle distributions and the resulting synchrotron, inverse Compton, and pion-decay emission in a largely self-consistent manner. The simulation is flexible and can be readily used with a wide range of parameters typical of γ-ray burst (GRB) afterglows. We describe some preliminary results for photon emission from shocks of different Lorentz factors and outline how the Monte Carlo simulation can be generalized and coupled to hydrodynamic simulations of GRB blast waves. We assume Bohm diffusion for simplicity but emphasize that the non-linear effects we describe stem mainly from an extended shock precursor where higher energy particles diffuse further upstream. Quantitative differences will occur with different diffusion models, particularly for the maximum CR energy and photon emission, but these non-linear effects should be qualitatively similar as long as the scattering mean-free path is an increasing function of momentum.

Key words: acceleration of particles – MHD – shock waves – turbulence – gamma-ray burst: general – cosmic rays.

1 INTRODUCTION

Efficient first-order *Fermi* shock acceleration (also called diffusive shock acceleration) is often suggested as a likely mechanism for converting the bulk kinetic energy of relativistic plasma flows into individual particle energy (e.g. Bykov & Treumann 2011; Bykov et al. 2012). However, many aspects of particle acceleration in relativistic shocks remain uncertain because of the inherent complexity of the process. The particle distributions are highly anisotropic and the magnetic turbulence, essential for acceleration to occur, must be self-generated and is extremely difficult to characterize (Lemoine & Pelletier 2003; Niemiec & Ostrowski 2006; Lemoine & Pelletier 2010; Reville & Bell 2014; Lemoine et al. 2014). These roadblocks can be overcome with particle-in-cell (PIC) simulations and intensive work has been done in this area (e.g. Nishikawa et al. 2007; Sironi & Spitkovsky 2011). However, current PIC simulations are computationally costly and have a limited dynamic range. The trans-relativistic regime, which may be important for GRB afterglows (e.g. Mészáros 2006; Ackermann et al. 2013) and some types of supernovae (e.g. Chakraborti et al. 2011), is less well explored either analytically or using PIC simulations (see, however, Casse, Marcowith & Keppens 2013).

In this paper we model the non-linear acceleration of electrons and ions (protons and He^{2+}) at relativistic collisionless shocks using a Monte Carlo simulation of first-order *Fermi* shock acceleration (e.g. Ellison & Double 2002; Ellison, Warren & Bykov 2013). The

⋆ E-mail: donald.warren@riken.jp (DCW); don_ellison@ncsu.edu (DCE); ambykov@yahoo.com (AMB)

steady-state Monte Carlo simulation parametrizes magnetic turbulence generation and particle diffusion, important approximations but ones that allow a large dynamic range, the simultaneous acceleration of ions and electrons (along with the radiation they produce), and a self-consistent determination of the shock structure. We believe this is the first attempt, apart from PIC simulations, to include electrons self-consistently with ions in a non-linear, relativistic, *Fermi* acceleration.

While it is well known that non-linear *Fermi* acceleration should preferentially inject and accelerate high mass-to-charge particles compared to protons in non-relativistic shocks (e.g. Ellison, Jones & Eichler 1981; Eichler 1984; Jones & Ellison 1991), to our knowledge this process has not been investigated in relativistic or trans-relativistic shocks until now. The non-relativistic 'A/Z' effect (A is the mass in units of the proton mass $m_{\rm p}$ and Z is the charge in units of the electron charge e) has been shown to be consistent with observations of diffuse ions accelerated at the Earth bow shock (Ellison, Moebius & Paschmann 1990) and has been used to model the shock acceleration of interstellar gas and dust, matching important aspects of the galactic cosmic ray (CR) abundances observed at Earth (e.g. Ellison, Drury & Meyer 1997; Meyer, Drury & Ellison 1997; Meyer & Ellison 1999; Rauch et al. 2010; Binns et al. 2014).

The A/Z enhancement we model is a purely kinematic effect. It depends on the following assumptions: (i) the acceleration process is efficient enough so the backpressure from accelerated particles noticeably modifies the shock precursor, (ii) all particles have a scattering mean-free-path of the approximate form

$$\lambda_{\rm mfp} = \eta_{\rm mfp} f_{\rm mfp}\,, \tag{1}$$

where $f_{\rm mfp}$ is an increasing function of local frame momentum p, as is generally assumed, and (iii) the normalization parameter $\eta_{\rm mfp}$ setting the 'strength' of scattering is similar for all particle species.

The simplest assumption for particle diffusion is that $f_{\rm mfp}$ equals the gyroradius, i.e. $f_{\rm mfp} = r_{\rm g} = pc/(ZeB)$. Then

$$\lambda_{\rm mfp} = \eta_{\rm mfp} r_{\rm g}\,, \tag{2}$$

and the precursor diffusion length for species i is

$$L_D^i \propto \eta_{\rm mfp}\gamma_i (A/Z) v_i^2\,. \tag{3}$$

Here γ_i (v_i) is the Lorentz factor (velocity) for species i, c is the speed of light, and B is the background magnetic field in Gauss used to scale $r_{\rm g}$. If $v_i \sim c$, then $\gamma \propto p/A$,

$$L_D^i \propto \eta_{\rm mfp}(A/Z)(p/A)\,, \tag{4}$$

and the precursor diffusion length for different A/Z ions, at the same momentum per nucleon, scales as A/Z.

Therefore, if $\eta_{\rm mfp}$ is similar for all species, at the same p/A, high A/Z particles will diffuse further into the upstream region, 'feel' a larger effective compression ratio in the modified shock structure than low A/Z particles, and gain a larger momentum boost in the next shock crossing. Since L_D^i increases with p/A, the modified shock precursor produces a distinctive concave spectral shape (e.g. Ellison & Eichler 1984) with high A/Z particles having a harder spectrum at any p/A than low A/Z particles (see Fig. 13). It is important to note that equation (2) is presented only as a simple baseline scattering mode. Small-scale turbulence, as generated by the Weibel instability at relativistic shocks (e.g. Nishikawa et al. 2006; Plotnikov, Pelletier & Lemoine 2011, 2013), in general leads to a different $\lambda_{\rm mfp} \propto p^2$ dependence (e.g. Jokipii 1971). In fact, the scattering process in relativistic shocks is almost certain to be more complicated than any simple power-law dependence for $\lambda_{\rm mfp}$, and $\eta_{\rm mfp}$ may be expected to have a momentum dependence as well (e.g. Achterberg et al. 2001; Kirk & Reville 2010; Sironi, Spitkovsky & Arons 2013; Lemoine et al. 2014). Our current results, with $\lambda_{\rm mfp} \propto r_{\rm g}$, display the essential physical effects that come about from the development of an extended shock precursor. As long as $\lambda_{\rm mfp}$ is an increasing function of p, and *Fermi* acceleration is efficient, the non-linear effects we describe should not depend qualitatively on the diffusion coefficient. Quantitatively, the momentum dependence of $\lambda_{\rm mfp}$ can strongly influence the maximum CR energy a given shock can produce and this, in turn, will influence the photon production. We are currently generalizing our Monte Carlo simulation to allow for a more complicated parametrization of $\lambda_{\rm mfp}$ over large energy and length scales. These future results will be compared against PIC simulations (e.g. Sironi et al. 2013). The results presented here provide a benchmark for future comparisons.

While the A/Z effect we describe can enhance the injection and acceleration of heavy ions compared to protons, for electrons with $A/Z \simeq 5.45 \times 10^{-4}$ it acts strongly in the opposite fashion. If only this kinematic effect is considered with equation (2), electrons will be dramatically less efficiently injected and accelerated than protons in non-linear *Fermi* acceleration.

Electron injection was considered in a non-relativistic Monte Carlo code similar to the one we use here in Baring et al. (1999). In that paper, in order to overcome the dramatic A/Z effect and allow electrons to be injected and accelerated with efficiencies large enough to be consistent with synchrotron and IC radiation observed in young supernova remnants (SNRs), the electron $\lambda_{\rm mfp}$ was set equal to a constant below some momentum, i.e. changing $\eta_{\rm mfp}$ selectively for electrons. This modification gave low-energy electrons a larger mean-free path than equation (2) would produce and allowed them to diffuse far enough upstream to overcome the shock smoothing effects. It was argued in Baring et al. (1999) that this simple modification was reasonably consistent with an electron injection model developed by Levinson (1992).

Here, we adopt a different approach. We keep equation (2), but transfer some fraction of the ram kinetic energy from ions to electrons as the particles first cross the viscous subshock. We note that a 'sharing' of energy between ions and electrons is clearly seen in recent PIC relativistic shock simulations (i.e. Sironi & Spitkovsky 2011; Sironi et al. 2013), and Plotnikov et al. (2013) give an analytical treatment of electromagnetic instabilities transferring energy to electrons in the precursor of relativistic shocks.

In the PIC simulations, electrons are heated in the precursor by interacting with turbulence generated mainly by backstreaming protons and obtain near equipartition with the protons before crossing the subshock. We mimic this effect by transferring a set fraction, $f_{\rm ion}$, of ion energy to electrons as particles first cross the subshock. While this simple energy transfer model is clearly an approximation, we feel it affords a straightforward way of using plasma physics information obtained from computationally intensive PIC simulations in a calculation that can model particle acceleration and photon emission consistent with the production of high-energy CRs in relativistic shocks.[1]

We recognize, of course, that collisionless shock formation, and particle injection and acceleration, is determined by more than kinematics alone. The self-generation of magnetic turbulence is critical

[1] Other descriptions of electron heating in relativistic plasmas include Gedalin et al. (2008), who investigate the effects of a cross-shock potential, and Kumar, Eichler & Gedalin (2015), who explore the electron heating behaviour of Weibel-induced current filaments in a 2D PIC simulation.

to the process (e.g. Bednarz & Ostrowski 1998; Lemoine & Pelletier 2003), particularly for relativistic shocks, and, as just mentioned, energy can be transferred between electrons and protons by wave–particle interactions that are essentially independent of the kinematics. Nevertheless, if *Fermi* acceleration is efficient, basic momentum and energy conservation demands that kinematics be taken into account and the shock precursor must be modified by the backpressure of accelerated particles.

In contrast to non-relativistic shocks, where shock acceleration can be directly tested against spacecraft observations (e.g. Ellison et al. 1990; Baring et al. 1997), *Fermi* acceleration in relativistic shocks is far less certain. Relativistic shocks cannot be directly observed with spacecraft, as can non-relativistic, heliospheric shocks, and the highly anisotropic particle distributions intrinsic to relativistic shocks make the self-generation of magnetic turbulence far more difficult to describe analytically. Despite this difficulty, intensive work continues (e.g. Lemoine & Pelletier 2010, 2011; Plotnikov et al. 2013). Furthermore, and again in contrast to non-relativistic shocks, the predictions for particle spectra and, therefore, photon signatures from relativistic shocks are highly uncertain. Sites harbouring relativistic shocks, such as GRBs, can often be successfully modelled with alternative acceleration mechanisms (e.g. magnetic reconnection in the case of GRBs; McKinney & Uzdensky 2012; Sironi, Petropoulou & Giannios 2015), weakening the link between *Fermi* acceleration theory and observation.

Despite this uncertainty, there is compelling evidence, primarily from PIC simulations (e.g. Hoshino et al. 1992; Kato 2007; Keshet et al. 2009; Sironi & Spitkovsky 2009; Nishikawa et al. 2011; Sironi & Spitkovsky 2011; Stockem et al. 2012), that relativistic shocks do accelerate electrons and protons beyond the initial kinematic boost from a single shock crossing. These simulations also highlight the role of the magnetization parameter, $\sigma_{\rm B}$, in *Fermi* acceleration, where

$$\sigma_{\rm B} = \frac{B_0^2}{4\pi n_0 m_{\rm p} c^2}\,, \tag{5}$$

B_0 is the upstream field, and n_0 is the number density (see Bykov & Treumann 2011, for an alternative definition of $\sigma_{\rm B}$).

Sironi et al. (2013) (see also Haugbølle 2011) show that perpendicular electron–ion shocks with Lorentz factors $\gamma_0 \lesssim 150$ inject and accelerate electrons and ions efficiently when $\sigma_{\rm B} \lesssim 3 \times 10^{-5}$. In these weakly magnetized plasmas, the self-generated turbulent field dominates the uniform B and the shock obliquity ceases to be important, an assumption often made in shock acceleration studies and one we make here with our plane-parallel shock assumption (cf. Fig. 2). Quantifying this lack of dependence on the obliquity is particularly important since ultra-relativistic shocks are essentially always highly oblique – the B-field component along the shock face can be highly compressed – and strongly magnetized oblique shocks are less able to inject and accelerate particles. We note that for typical interstellar medium (ISM) conditions, $B_0 \sim 3$ μG, $n_0 \sim 0.03$ cm^{-3}, and so $\sigma_{\rm B} \sim 10^{-9}$. This value is orders of magnitude below the threshold reported by Sironi et al. (2013), suggesting that ultra-relativistic shocks propagating in the normal ISM may be able to inject and accelerate electrons and ions far more efficiently than previously believed, regardless of the shock obliquity. We note that for non-relativistic shocks the plasma $\beta \equiv n_0 k_{\rm B} T_0/(B_0^2/8\pi)$ is the relevant parameter rather than equation (5) and oblique geometry may be important for typical ISM parameters (e.g. Orlando et al. 2011). Here $k_{\rm B}$ is Boltzmann's constant and T_0 is the ambient unshocked temperature.

Given that weakly magnetized relativistic shocks can inject particles, the maximum energy these particles obtain in a given shock remains uncertain, although arguments presented by Sironi et al. (2013) suggest that the acceleration reaches a maximum, $E_{\rm max}$, where $E_{\rm max}/(\gamma_0 m_{\rm p} c^2) \sim \sigma_{\rm B}^{-1/4}$. While this can be a substantial energy (for $\sigma_{\rm B} = 3 \times 10^{-5}$, $E_{\rm max} \sim 0.2$ TeV), it is well below what is often assumed in suggesting that relativistic shocks may produce ultra-high-energy CRs (e.g. Keshet & Waxman 2005). Here we simply parametrize the maximum particle energy by setting a maximum shock size with a free escape boundary (FEB).[2]

Next we describe the generalization of the Monte Carlo code used in Ellison et al. (2013) to include the injection and acceleration of electrons simultaneously with ions. The non-linear shock structure is calculated including thermal leakage injection and the backreaction from all species. Full particle spectra are determined at various positions relative to the subshock, along with the distributions of particles that escape at upstream and downstream FEBs. For given values of the ambient density, magnetic field, and background photon field, we calculate the synchrotron emission using equation (6.7a) in Rybicki & Lightman (1979), the inverse Compton (IC) emission using equation (9) in Jones (1968), and the pion-decay emission using parametrizations given by Kamae et al. (2006, 2007) and Kelner, Aharonian & Bugayov (2009). For the pion-decay from He^{2+}, we use the scaling relation given in Baring et al. (1999). Once the emission is determined in the local frame it is transformed to the observer (i.e. ISM) frame.

We note that radiation losses for electrons are only considered during the acceleration process. Once accelerated, we assume the electrons radiate without further losses. This so-called 'thin target' approximation, where the radiation length is assumed to be larger than the region between the upstream and downstream FEBs, is adequate for the steady-state examples given here and can be relaxed in models of evolving GRBs (see Warren 2015).

2 MODEL

We assume the basic Monte Carlo scattering model, as described in Ellison et al. (2013) for protons, applies equally to electrons and heavy ions. If so, all that is needed to describe the injection and acceleration of electrons is a parameter describing the transfer of energy from ions to electrons, mimicking the effect seen in PIC simulations of relativistic shocks (see Sironi & Spitkovsky 2011).

Full details of the particle scattering model, thermal leakage injection, and the method for obtaining a self-consistent shock precursor structure when *Fermi* acceleration and particle escape occur are given in section 2 of Ellison et al. (2013). In Ellison et al. (2013), we also fully explain the caveats needed when applying the Monte Carlo model to relativistic shocks and show how the approximations required in the Monte Carlo model compare with previous Monte Carlo work and with more fundamental PIC simulations.

We describe particle transport by assuming the mean-free path, $\lambda_{\rm mfp}$, is given by equation (2) with $\eta_{\rm mfp} = 1$, i.e. Bohm diffusion.[3] As

[2] A FEB is a position beyond which particles are assumed to decouple from the shock. Any actual shock will be finite in extent and at some point high-energy particles will obtain diffusion lengths comparable to the shock size and stream freely away. Our FEBs model a finite shock size within our steady-state, plane-parallel approximation.

[3] We note that since all lengths in the steady-state code are scaled with $r_{\rm g0} = \eta_{\rm mfp} m_{\rm p} u_0 c/(eB_0)$, where u_0 is the shock speed, our results are independent of $\eta_{\rm mfp}$ except for the absolute normalization of the particle spectra, i.e. the number of particles within a physical region scales as $\eta_{\rm mfp}$. In our

mentioned above, while there is some theoretical and observational support for Bohm diffusion from X-ray afterglows (e.g. Sagi & Nakar 2012), most theoretical work suggests a stronger momentum dependence, i.e. $\lambda_{\rm mfp} \propto p^2$ (e.g. Plotnikov et al. 2011). We use equation (2) for convenience and as a baseline for future work which will assume more complicated (and, hopefully, more realistic) forms for $\lambda_{\rm mfp}$. The particle is moved for a time $\delta t \ll t_{\rm c}$, where $t_{\rm c} = \lambda_{\rm mfp}/v_i$ is the 'collision time', i.e. the average time measured in the local frame needed for the particle to accumulate deflections on the order of 90°. The second scattering parameter, $N_{\rm g}$, determines the 'fineness' of scattering through an equation for the maximum deflection, $\delta\theta_{\rm max}$, a particle can experience in a pitch-angle interaction event after each δt, i.e.

$$\delta\theta_{\rm max} = \sqrt{12\pi/(\eta_{\rm mfp} N_{\rm g})}\,. \quad (6)$$

Here, $N_{\rm g} = \tau_{\rm g}/\delta t$ is the number of gyro-time segments δt dividing a gyro-period $\tau_{\rm g} = 2\pi r_{\rm g}/v_i$, and we note that equation (6) applies even if particles move rapidly between inertial frames, as is normally the case for relativistic shocks. In each scattering event, the scattering is assumed to be isotropic and elastic in the local plasma frame (LPF).

Large values of $N_{\rm g}$ imply fine scattering while small values imply that the particle momentum will suffer relatively large deviations in direction in each pitch-angle scattering event (e.g. Summerlin & Baring 2012). In all examples here, $N_{\rm g}$ is large enough to saturate and produce fine-scattering results that do not change substantially as $N_{\rm g}$ is increased further.[4] It is important to note that while we can simply parametrize particle transport with the assumption given by equation (2) and the two parameters $\lambda_{\rm mfp}$ and $N_{\rm g}$, this assumes that magnetic fluctuations with correlation lengths on the order of $L_{\rm c} = 2\pi\eta_{\rm mfp} r_{\rm g}/N_{\rm g}$ exist with sufficient power to produce this scattering throughout the shock. We make no claim of self-consistently determining the magnetic turbulence needed to produce the diffusion implied by equation (2).[5]

All of the above is applied equally to electrons and ions and this parametrization yields injection rates and acceleration efficiencies that depend on the A/Z ratio. We note that particle injection from shock-heated thermal particles (our thermal leakage injection model) occurs directly from the above assumptions. Regardless of the shock speed, virtually all cold, thermal, unshocked particles obtain a velocity greater than the downstream bulk flow speed when they first scatter in the downstream region and the flow becomes subsonic. Depending on their angular distribution, these particles have a finite probability of scattering back upstream where they will be further accelerated. In the Monte Carlo code, the injection efficiency is determined stochastically as some particles manage to scatter back upstream with an angular distribution determined solely from the scattering model with no additional assumptions or parameters other than that the subshock is assumed to be transparent for back-scattering particles.

To this we add one additional parameter, $f_{\rm ion}$, i.e. the fraction of far upstream ion ram kinetic energy transferred to electrons. The ion ram kinetic energy is defined as $(\gamma_0 - 1)m_i c^2$, where m_i is the ion mass, $\gamma_0 = [1 - (u_0/c)^2]^{-1/2}$ is the far upstream shock Lorentz factor, and u_0 is the far upstream (i.e. unmodified) shock speed. When an ion crosses the subshock from upstream to downstream for the first time, energy equal to $f_{\rm ion}(\gamma_0 - 1)m_i c^2$ is removed from it. The total ion energy transferred is $f_{\rm ion}\sum_i(\gamma_0 - 1)N_i m_i c^2$, where the sum is over the ion species and N_i is the number of i-ions injected far upstream. This ion energy is divided equally among electrons and added to their energy as they cross the subshock into the downstream region for the first time. The parameter $f_{\rm ion}$ can increase electron injection substantially as we show below.

3 RESULTS

We approximate the geometry of a relativistic afterglow shock moving in a jet as shown in Fig. 1. Details of this situation are shown in Fig. 2, where we show the additional approximations for this preliminary work that the shock is locally plane, the distances to the upstream or downstream FEBs ($L_{\rm UpS}$ and $L_{\rm DwS}$) measured from

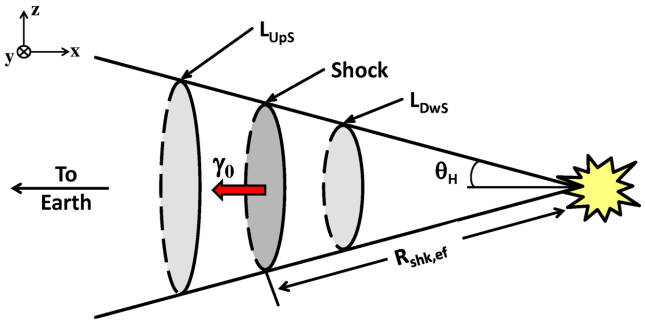

Figure 1. Schematic, not-to-scale representation of a relativistic shock embedded in a conical jet, propagating with a Lorentz factor γ_0 into material at rest. The region of interest is delimited by $L_{\rm UpS}$ and $L_{\rm DwS}$; outside of this region, we assume the particles decouple from the shock and we ignore any emission resulting from them. The jet opening half-angle is θ_H, and the shock has propagated a distance $R_{\rm shk,\,ef}$ in the explosion (or ISM) frame. We only consider emission directed along the jet to an observer at Earth.

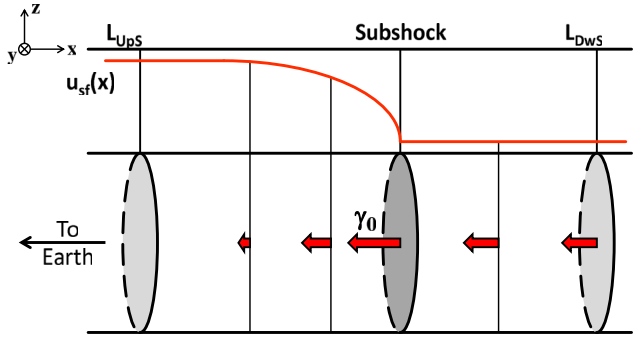

Figure 2. This detail focuses on the volume between $L_{\rm UpS}$ and $L_{\rm DwS}$. The upper panel shows the shock-frame plasma velocity profile. The lower panel shows the ISM-frame velocity at selected points in the shock structure, varying from 0 for $x < L_{\rm UpS}$ to u_0 just upstream from the subshock at $x = 0$. Note that we assume the shock is locally plane and that $L_{\rm UpS}$ and $L_{\rm DwS}$ are small compared to $R_{\rm shk,\,ef}$ as illustrated in Fig. 1.

plane-parallel approximation, the field throughout the shock retains the far upstream value B_0.

[4] We note that all of our fully relativistic, unmodified shock examples yield the well-known power-law $dN/dp \propto p^{-2.23}$ (e.g. Bednarz & Ostrowski 1998; Kirk et al. 2000; Keshet & Waxman 2005) (see Fig. 3). Harder spectra can be obtained with large-angle scattering, i.e. small values of $N_{\rm g}$ (e.g. Ellison & Double 2004; Summerlin & Baring 2012), or other ad hoc assumptions (e.g. Schlickeiser 2015) but care must be taken to account for NL effects when the power-law index is less than 2 (see fig. 13 in Ellison et al. 2013).

[5] We note that a non-linear, non-relativistic Monte Carlo code which does include the self-generation of magnetic turbulence has been developed (e.g. Vladimirov, Bykov & Ellison 2008, 2009; Bykov et al. 2014).

Table 1. Model parameters.

Model[a]	Type[b]	γ_0	$f_{\rm ion}$	B_0 [μG]	$L_{\rm UpS}$ $r_{\rm g0}$	$L_{\rm DwS}$ $r_{\rm g0}$	$R_{\rm RH}$	$R_{\rm tot}$	$N_{\rm g}$	$\epsilon_{\rm H}$[c]	$\epsilon_{\rm He}$	$\epsilon_{\rm el}$
A	UM	10	0	100	10^4	...	3.02	3.02	2000	...	...	...
B	UM	10	0.15	100	10^4	...	3.02	3.02	2000	...	...	...
C	UM	10	0.15	3	10^3	10^3	3.02	3.02	2000	...	...	...
D	UM	10	0.1	100	300	10^3	3.02	3.02	2000	...	...	...
E	NL	10	0.1	100	300	10^3	3.02	3.02	2000	0.60	0.30	0.10
F	NL	10	0.4	100	300	10^3	3.02	3.02	2000	0.36	0.20	0.44
G	UM	1.5	0.1	100	300	10^3	3.53	3.53	200	...	...	...
H	NL	1.5	0.1	100	300	10^3	3.53	3.9 ± 0.4	200	0.52	0.27	0.08
I	UM	30	...	100	300	10^4	3.00	3.00	10^4	...	...	...
J	NL	30	...	100	300	10^4	3.00	3.00	10^4	0.66	0.34	...

Notes. [a]Models A, B, and C have $n_{\rm p} = n_e = 1$ cm^{-3} with no helium. Models D– H have $n_{\rm p} = 1$ cm^{-3}, $n_{\rm He} = 0.1$ cm^{-3}, and $n_e = 1.2$ cm^{-3}. Models I and J have $n_{\rm p} = 1$ cm^{-3} and $n_{\rm He} = 0.1 n_{\rm p}$ without electrons. The far upstream temperature is 10^6 K in all cases and all models have $\eta_{\rm mfp} = 1$.
[b]In the non-linear (NL) models the shock structure is determined self-consistently. The unmodified (UM) models have a discontinuous shock structure with no shock smoothing.
[c]For self-consistent NL models, this is the fraction of total energy placed in all particles with energies above 100 MeV as measured in the shock frame.

the subshock are small enough so the jet cone is approximately a cylinder in the region surrounding the shock, and the diameter of the 'cylinder' is large enough so particle escape out the sides of the cone is negligible. The cone material outside the upstream FEB is assumed to be stationary, i.e. it is in the local ISM or explosion frame. Outside of the region between $L_{\rm UpS}$ and $L_{\rm DwS}$ we assume all accelerated particles have decoupled from the plasma and we ignore any emission they might produce. A more realistic GRB afterglow model following the evolution of a jet shock is given in Warren (2015).

With these approximations we calculate the shock structure and particle spectra for a given set of parameters, as listed in Table 1. First we consider unmodified (UM) shocks where the backreaction of the accelerated particles on the shock structure is ignored. We note an essential difference between unmodified shocks and test-particle (TP) ones. A TP shock is one where the injection and acceleration efficiencies are low enough so the backpressure from accelerated particles can be ignored. In the TP case, to the limit of total energy placed in accelerated particles, momentum and energy can be conserved without modifying the shock structure. Our thermal leakage injection model is efficient enough so TP shocks are never produced for the parameters we use here. In our UM examples, particles are injected and accelerated efficiently but the effect of shock accelerated particles on the shock structure is ignored. This provides a direct comparison to non-linear (NL) shocks, where momentum and energy are conserved. Our main point in this paper is that, if the acceleration is efficient, the shock must be modified by the accelerated particles.

While we do not consider TP shocks explicitly, the superthermal particle fluxes and photon emission from our UM examples can be simply re-scaled to a TP result. For example, if a TP result is defined as one where superthermal particles contain $\leq$1 per cent of the total energy flux, so energy flux will be conserved to within 1 per cent, our UM superthermal particle and photon emission need to be reduced by a factor $N_{\rm TP} \geq 100 \times [F_{\rm en}(x > 0)/F^0_{\rm en}]$, where $F^0_{\rm en}$ is the far upstream energy flux and $F_{\rm en}(x > 0)$ is the UM downstream energy flux. For the UM $\gamma_0 = 10$ examples we show below $F_{\rm en}(x > 0)/F^0_{\rm en} \sim 2$.

3.1 Unmodified (UM) examples

In Fig. 3 we show number spectra, dN/dp, calculated just downstream from an unmodified shock with $\gamma_0 = 10$. The solid and dotted black curves are protons and the red curves are electrons. The dotted curves were calculated for $f_{\rm ion} = 0$, while the solid curves were calculated with $f_{\rm ion} = 0.15$, i.e. 15 per cent of the proton ram kinetic energy is transferred to electrons as particles first cross $x = 0$

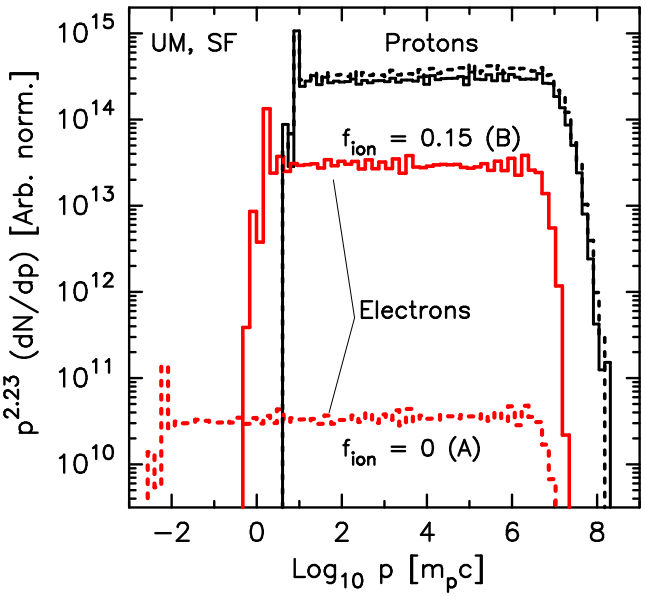

Figure 3. Protons (black curves) and electrons (red curves) from UM shocks with different $f_{\rm ion}$ as indicated. These spectra, multiplied by $p^{2.23}$, are calculated downstream from the shock, in the shock frame, and have arbitrary overall normalization although the relative normalization between electrons and protons is absolute. An upstream FEB of $L_{\rm UpS} = -10^4\, r_{\rm g0}$ was used with no downstream FEB, i.e. a probability-of-return calculation was used to simulate an infinite downstream region. In Table 1 the $f_{\rm ion} = 0$ case is Model A and the $f_{\rm ion} = 0.15$ case is Model B.

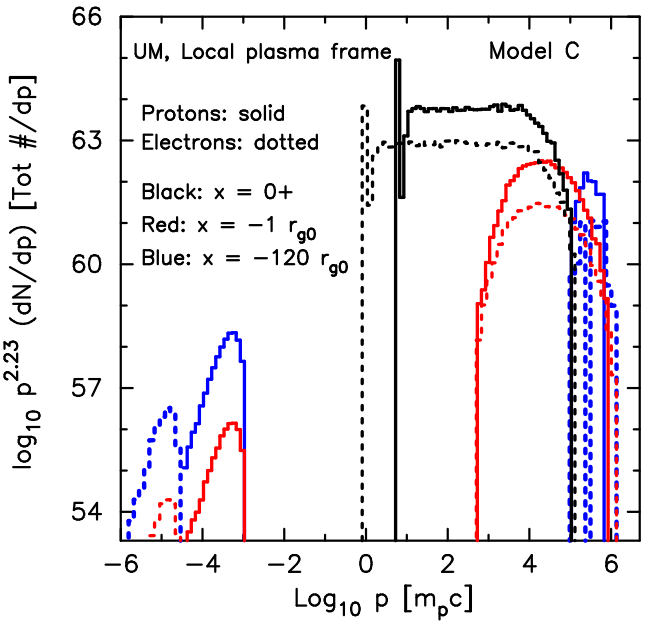

Figure 4. Proton and electron spectra (as labelled and multiplied by $p^{2.23}$) with $f_{\rm ion} = 0.15$. These spectra are measured in the LPF and are normalized to the total number of particles in a given region, as indicated in Fig. 2. The shock acceleration is limited by an upstream FEB at $L_{\rm UpS} = -1000\, r_{\rm g0}$, and a downstream FEB at $L_{\rm DwS} = +1000\, r_{\rm g0}$.

headed downstream.[6] Since all particles injected far upstream are non-relativistic, the transformation from upstream to downstream frames strongly favours more massive particles in the first shock crossing. This results in the strong depression of electrons relative to H^+. Once all particles become relativistic they are treated equally and obtain similar power laws, i.e. the UM shocks in Fig. 3 show the canonical $dN/dp \propto p^{-2.23}$ power law above the 'thermal' peak and below the high momentum cutoff. For the protons, the cutoff at $\sim 10^7\, m_{\rm p}c$ is produced by an upstream FEB at $L_{\rm UpS} = -1 \times 10^4\, r_{\rm g0}$, where $r_{\rm g0} = \eta_{\rm mfp} m_{\rm p} u_0 c/(eB_0)$. The electrons cut off at a lower momentum ($\sim 2 \times 10^6\, m_{\rm p}c$) due to radiation losses. Without radiation losses, the electrons would obtain the same $p_{\rm max}$ as protons since $p_{\rm max}$ scales as Z. The normalization of the electron spectra shows the dramatic effect of $f_{\rm ion}$: the e/p ratio is increased by nearly three orders of magnitude with $f_{\rm ion} = 0.15$. The proton normalization is only slightly influenced by $f_{\rm ion}$.

To save computation time, the models in Fig. 3 used a probability-of-return calculation instead of a downstream FEB. This mimics an infinite downstream region and allows rapid acceleration to high energies (see Ellison, Baring & Jones 1996, for a discussion of the probability of return calculation). In Fig. 4 we show spectra from an UM shock measured in the LPF with both upstream and downstream FEBs. While both FEBs are present, typically one (the shorter, measured in diffusion lengths) will determine the maximum momentum $p_{\rm max}$. For Fig. 4, both $L_{\rm UpS}$ and $L_{\rm DwS}$ are $1 \times 10^3\, r_{\rm g0}$ from the subshock, but $L_{\rm DwS}$ determines $p_{\rm max}$ since it is much more difficult for particles to stream away from the shock in the upstream region with $\gamma_0 = 10$.

[6] We refer to the sharp drop in $u(x)$ that occurs at $x \simeq 0$ as the subshock (see Figs 5 and 10). For an unmodified shock, there is no distinction between the shock and subshock.

The FEBs also determine the total number of particles accelerated (as indicated in Fig. 2) and the dN/dp spectra in Fig. 4 are normalized to the total particle number in a region surrounding an observation position x (the position is indicated in Fig. 4). While the particular number of accelerated particles in these examples is arbitrary,[7] it is important to note that the Monte Carlo code determines the absolute number of accelerated particles, and subsequent radiation, for any given set of environmental and shock parameters, including $f_{\rm ion}$. As long as $\gamma_0 \gg 1$, the large majority of accelerated particles will be in the downstream region since it is difficult for particles to stream upstream into the shock precursor. This is reflected in the higher normalizations of the black curves, measured at $x = 0+$ (i.e. downstream), compared to the red or blue curves, measured in the shock precursor at $x = -1\, r_{\rm g0}$ and $x = -120\, r_{\rm g0}$, respectively.

Besides the downstream FEB and normalization, the spectra in Fig. 4 differ from those in Fig. 3 in that they are shown in the LPF and they include spectra calculated upstream from the subshock (red and blue curves), as well as downstream (black curves). The effect of the Lorentz transformation from the shock to the LPF is clearly indicated by the high-momentum upstream spectra (red and blue curves) which extend to higher momentum than the downstream spectra. Relative to the subshock, the upstream plasma frame moves with $\gamma_0 = 10$, while the downstream plasma frame moves with $\gamma_2 = [1 - (u_2/c)^2]^{-1/2} \simeq 1.06$. Here u_2 is the downstream bulk plasma speed measured in the shock frame.

3.2 Non-linear examples, $\gamma_0 = 10$

In Fig. 5 we show the structure of a shock where the backpressure from accelerated protons, He^{2+}, and electrons is taken into account. For this example, $f_{\rm ion} = 0.1$, and the electron pressure contributes to the determination of the self-consistent shock structure. Here $L_{\rm UpS} = -300\, r_{\rm g0}$ and $L_{\rm DwS} = +1000\, r_{\rm g0}$. In the top panels, the solid (black) curve is the bulk flow speed, $u(x)/u_0$, and the dot–dashed (blue) curve is $\gamma(x)\beta(x)/(\gamma_0\beta_0)$, where $\beta(x) = u(x)/c$, $\gamma(x) = [1 - \beta(x)^2]^{-1/2}$, and $\beta_0 = u_0/c$. The dashed (red) curve is $u(x)/u_0$ for the UM case. The lower panels show the momentum and energy fluxes for the NL case (solid black curves), as well as for the UM case (dashed red curves). All curves are normalized to far upstream values. Without shock smoothing, the downstream momentum and energy fluxes are nearly a factor of 2 out of conservation.

We note that in non-relativistic and trans-relativistic shocks, the smoothing required for momentum and energy conservation is accompanied by an increase in the overall shock compression ratio above the Rankine–Hugoniot value, i.e. $R_{\rm tot} > R_{\rm RH}$ (e.g. Berezhko & Ellison 1999). The overall compression ratio is defined as $R_{\rm tot} = u_0/u_2$ and the subshock compression ratio is $R_{\rm sub} = u_1/u_2$. Here, u_2 is the bulk plasma speed downstream from the subshock and u_1 is the plasma speed just upstream of the viscous subshock, both measured in the shock rest frame.[8]

[7] The normalization of the spectra in Fig. 4 (and Figs 6 and 11) depends on the opening angle and length of the jet, the ambient number density, and the positions of the FEBs (see Warren 2015, for a full discussion).

[8] As seen in Fig. 5, the definition of u_1 is imprecise because the Monte Carlo solution allows for a smooth decrease in the precursor speed into the downstream region. Part of the increase in $R_{\rm tot}$ is due to escaping particles acting to soften the equation of state for the plasma that remains coupled to the shock system. The remainder of the increase is caused by the ratio of specific heats for particles downstream of the shock: as the shock speed increases, the particles receive more energy from the first shock crossing,

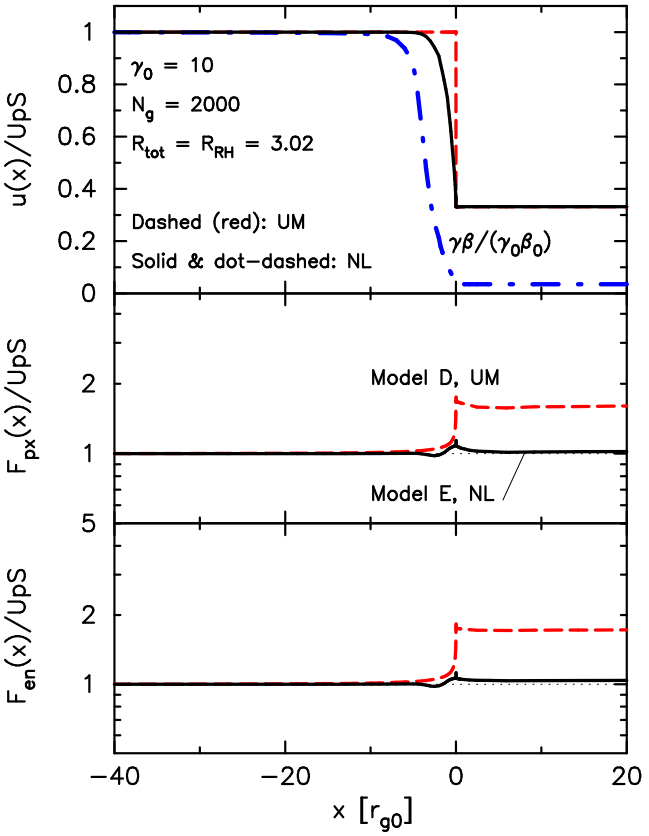

Figure 5. The top panel shows the shock structure for the unmodified case (dashed red curve, Model D) and the non-linear case (solid black and dot–dashed blue curves, Model E). The solid (black) and dashed (red) curves in the top panel are the flow speed $u(x)/u_0$ while the dot–dashed (blue) curve is $\gamma(x)\beta(x)/(\gamma_0\beta_0)$, where $\gamma(x)\beta(x)$ scales as 1/density for the non-linear shock. The middle and bottom panels show the momentum and energy fluxes, respectively, normalized to far upstream values. Note that three particle species, protons, He^{2+}, and electrons, are included in determining the self-consistent shock structure.

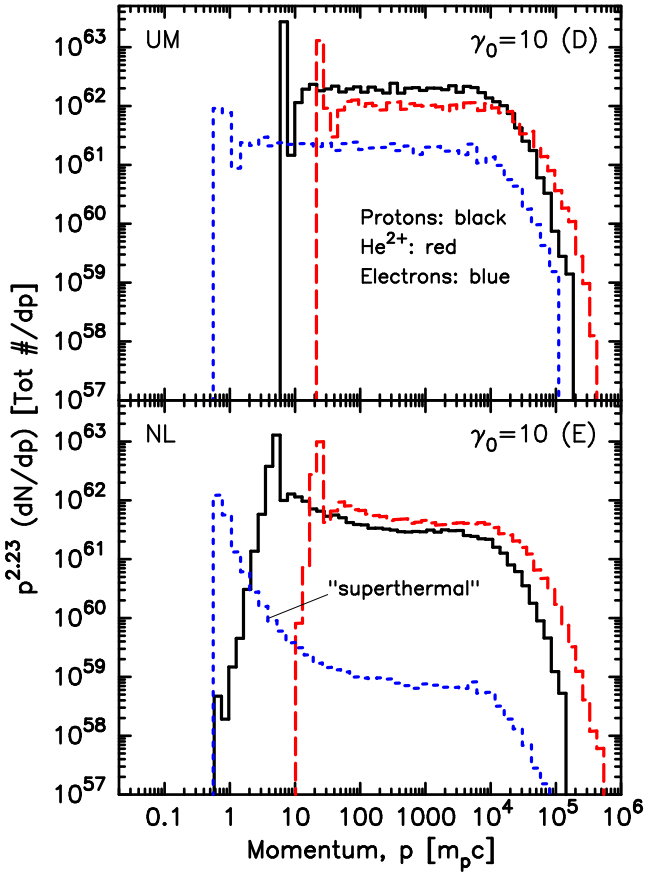

Figure 6. Downstream, LPF spectra for the unmodified shock shown in Fig. 5 (top panel, Model D) and the non-linear shock shown in Fig. 5 (bottom panel, Model E). Note the pronounced 'superthermal' tail on the electron distribution.

The top panel in Fig. 6 shows downstream proton, He^{2+}, and electron spectra for the UM shock (dashed curves in Fig. 5). The bottom panel shows these spectra from the non-linear shock. All parameters are the same for these two cases – the only difference is that momentum and energy are conserved in the NL case.

The effects of the smooth shock structure are clearly evident. In the NL case, the downstream spectra are noticeably curved and less intense, as is necessary to conserve energy and momentum. Significantly, the electrons are more modified than the protons or He^{2+} and the e/p ratio, in the quasi-power law portion of the spectra, drops by more than an order of magnitude. With $f_{ion} = 0$, e/p would have dropped by several more orders. This difference is a direct result of our scattering assumption, i.e. equation (2). The electrons, with their small A/Z, feel the effects of the smooth shock more acutely than the heavier ions and are less efficiently injected and accelerated until they reach $p \gtrsim 10\, m_p c$. In sources where electrons are assumed to have a large fraction of the energy budget, the efficiency for accelerating electrons cannot be orders of magnitude less than it is for protons. Therefore, energy must be transferred from heavy particles to electrons with a reasonable efficiency if *Fermi* acceleration is to be important (e.g. Sironi & Spitkovsky 2011; Sironi et al. 2013).

The heavier He^{2+}, with $A/Z = 2$, is accelerated more efficiently than protons; the He^{+2}/p ratio above $\sim 100\, m_p c$ goes from $He^{+2}/p < 1$ in the UM shock to $He^{+2}/p > 1$ in the NL shock (see Fig. 13). This is particularly significant at the high-momentum cutoff. The A/Z effect is discussed in more detail in Section 3.6. For Model E in Fig. 6, the fraction of total ram kinetic energy placed in particles of 100 MeV or greater is $\epsilon_H = 0.60$, $\epsilon_{He} = 0.30$, and $\epsilon_{el} = 0.10$, for protons, He^{2+}, and electrons, respectively (see Table 1 where it is noted that these fractions are measured in the shock frame).

The effects of shock smoothing also show up in the broadening and shift to lower momentum of the 'thermal' peaks, as seen in the bottom panel of Fig. 6. Of particular interest is the pronounced 'superthermal' tail the electrons obtain in the NL case. If synchrotron-self-absorption (SSA) is unimportant, this can produce a notable effect in the synchrotron emission, as we discuss next.

the average particle approaches relativistic energies, and the ratio of specific heats drops from 5/3 → 4/3. For fully relativistic shocks, however, $R_{tot} \simeq R_{RH}$ (Double et al. 2004); there is minimal particle escape, and the downstream ratio of specific heats is already ∼4/3 and so cannot decrease further. The compression ratio in Fig. 5 reflects this invariance, as it is the same in the unmodified and non-linear cases.

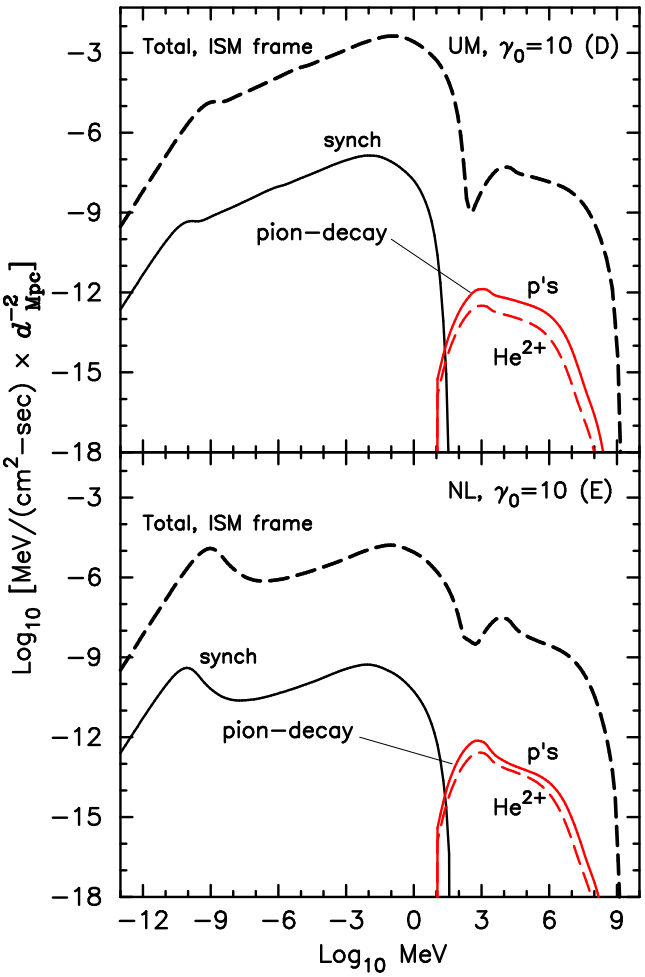

Figure 7. Photon emission for the UM (Model D) and NL (Model E) shocks shown in Figs 5 and 6. The dashed (black) curves are the total emission transformed to the ISM frame for an observer at $D_{\rm obs} = -d_{\rm Mpc}$ Mpc, at an angle within $1/\gamma_0$ from the shock normal. The lower synchrotron and pion-decay curves in each panel show emission calculated in the LPF and summed over the shock from $L_{\rm UpS} = -300\,r_{\rm g0}$ to $L_{\rm DwS} = +1000\,r_{\rm g0}$. The dashed (red) pion-decay curves are the LPF emission from He^{2+}.

3.3 Photon emission, $\gamma_0 = 10$

In Fig. 7 we show the photon emission produced by the shocks described in Figs 5 and 6. As in Fig. 6, the top panel is for the unmodified shock and the bottom panel is for the non-linear shock – all other parameters are the same. The curves labelled synchrotron and pion-decay show isotropic emission calculated in the LPF summed over the regions between the upstream and downstream FEBs (i.e. between $x = -300\,r_{\rm g0}$ and $x = +1000\,r_{\rm g0}$) as indicated in Fig. 2. These are the fluxes that would be observed at a distance $d_{\rm Mpc}$ Mpc if no Lorentz transformations were required. Here, $d_{\rm Mpc}$ is the distance in Mpc. Of course, the particle distributions will not be isotropic in the ISM frame, and Lorentz transformations are required. The dashed (black) curves show the total emission from synchrotron, IC, and pion-decay transformed to the ISM frame and seen by an observer at $D_{\rm obs} = -d_{\rm Mpc}$ Mpc within an angle $1/\gamma_0$ from the shock normal.

The shock simulation is done in the shock rest frame. To obtain the LPF synchrotron and pion-decay spectra we first transform the particle spectra to the LPF taking into account the anisotropies introduced by the relativistic flow. We then calculate the photon emission in the LPF assuming it is produced isotropically. This is reasonable for the synchrotron emission since we implicitly assume the background magnetic field is highly turbulent, and the synchrotron photons should be produced isotropically as the electrons spiral in the turbulent field. It is also a good approximation for the pion-decay emission since the protons and He^{2+} ions interact with the local plasma and produce pions that can become isotropic in the LPF before emitting a γ-ray.

From this isotropic emission, we obtain the flux in the ISM frame ahead of the shock by employing the standard Doppler shift and Lorentz transformations (e.g. Kumar & Zhang 2015). For an observer at $D_{\rm obs} = -d_{\rm Mpc}$ Mpc, within an angle $\theta_{\rm obs} = 1/\gamma_0$ from the jet direction, these give a boost to the energy flux $\propto \mathcal{D}^4$, where $\mathcal{D} = \gamma(x)[1 + \beta(x)\cos\theta_{\rm obs}]$ is the Doppler factor at position x relative to the subshock. One factor of $\mathcal{D}$ comes from the Doppler shift, one from time dilation, and two from the relativistic beaming. Here $\gamma(x)$ and $\beta(x)$ are measured relative to the ISM frame and will be different for each region between the upstream and downstream FEBs as shown in Fig. 2. Far upstream $\mathcal{D} = 1$, while downstream for $\gamma_0 = 10$ and $R_{\rm tot} \simeq 3.02$, $\mathcal{D} \simeq 14$.

Since the cosmic microwave background (CMB) photons are nearly isotropic in the ISM frame, we calculate the IC emission in a different fashion.[9] We first transform the electron distribution into the ISM frame keeping the two-dimensional anisotropy inherent in our plane-parallel shock simulation. We then calculate the emission directed towards the observer at $D_{\rm obs} = -d_{\rm Mpc}$ Mpc using equation (9) in Jones (1968). The assumption here is that the relativistic electrons produce strongly beamed emission, so only those electrons directed towards the observer contribute to the observed flux. In Fig. 7, the dashed (black) curves contain the full observed flux from emission produced over the modified shock structure and transformed to the ISM frame for an observer within $1/\gamma_0$ from the jet axis (i.e. towards $+x$ in Fig. 2). The IC emission is part of this sum.

The effects from shock smoothing on the particle distributions (Fig. 6) produce corresponding changes in the photon emission. Since electrons are suppressed more than ions in the NL shock, the synchrotron and IC emission drops more than pion-decay between the UM and NL cases. In contrast, the pion-decay from He^{2+} (dashed red pion-decay curve) is increased relative to that from protons by the A/Z effect. The 'thermal' peaks near 1 $m_{\rm p}c$ for electrons, and near 10 $m_{\rm p}c$ for protons and He^{2+}, show up as clear peaks in the synchrotron and pion-decay emission at $E \sim 10^{-11}$ and 10^3 MeV, respectively. This is particularly significant for the synchrotron emission near 10^{-9} MeV. The NL curvature in the particle spectra shows clearly in the individual components and remains strongly evident in the summed flux (bottom panel of Fig. 7).

3.4 Non-linear, $\gamma_0 = 10$, variation of $f_{\rm ion}$

While we have used $f_{\rm ion} = 0.1$ in our NL Model E, the PIC simulations of Sironi et al. (2013) show examples where ~40 per cent of the energy in accelerated particles ends up in electrons (see fig. 11 in Sironi et al. 2013). In Fig. 8 we compare particle spectra, and in Fig. 9 the total observed energy flux, for $f_{\rm ion} = 0.1$ (Model E) and $f_{\rm ion} = 0.4$ (Model F). The flux between $\sim 10^{-9}$ MeV and ~1 GeV

[9] We only consider CMB photons here for simplicity – the techniques we present can be generalized to include IC emission from other photon fields including synchrotron self-Compton photons if the jet parameters warrant it.

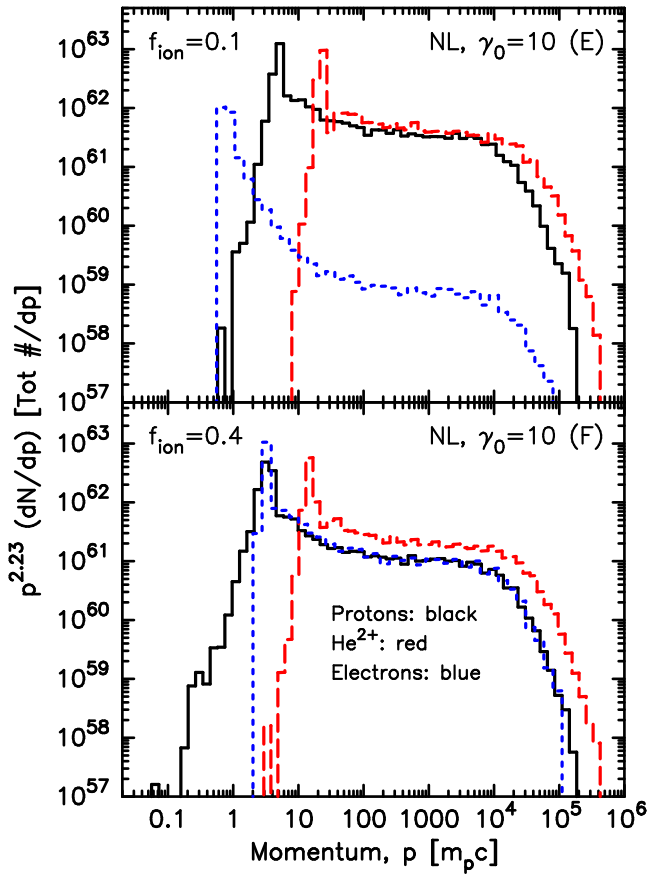

Figure 8. Non-linear downstream LPF spectra for Model E ($f_{\rm ion} = 0.1$) and Model F ($f_{\rm ion} = 0.4$). In both panels the solid (black) curves are protons, the dashed (red) curves are He^{2+}, and the dotted (blue) curves are electrons.

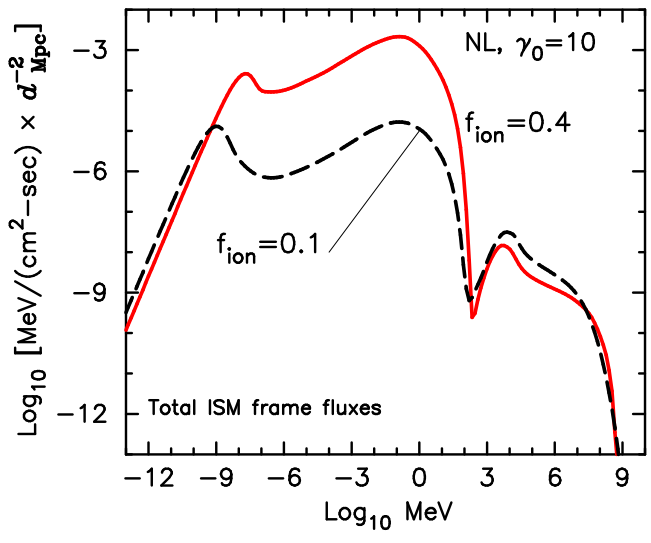

Figure 9. Total observed energy flux for NL Models E ($f_{\rm ion} = 0.1$) and F ($f_{\rm ion} = 0.4$).

is ∼100 times greater for the $f_{\rm ion} = 0.4$ case, with a much smaller decrease in the GeV–TeV emission. The $f_{\rm ion} = 0.4$ example shows the curved spectral shape that results from the NL shock smoothing but it is less pronounced between 10^{-9} and 1 MeV than for $f_{\rm ion} = 0.1$. In the GeV–TeV range, the curvature is slightly greater than for $f_{\rm ion} = 0.4$.

With $f_{\rm ion} = 0.4$, the energy distribution above 100 MeV in protons, He^{2+}, and electrons is $\epsilon_{\rm H} = 0.36$, $\epsilon_{\rm He} = 0.20$, and $\epsilon_{\rm el} = 0.44$, respectively; nearly 50 per cent of the ram kinetic energy goes into 100 MeV or greater electrons, as measured in the shock frame. The large difference in electron normalization between the $f_{\rm ion} = 0.1$ and 0.4 cases comes about mainly from the NL shock smoothing effects the electrons with $f_{\rm ion} = 0.1$ receive. When $f_{\rm ion} = 0.4$, the lowest energy downstream electrons that cross back upstream have a long enough diffusion length so they feel a large effective compression ratio. Non-linear effects reduce the electron acceleration more for $f_{\rm ion} = 0.1$ than for $f_{\rm ion} = 0.4$.

3.5 Trans-relativistic, $\gamma_0 = 1.5$

As described in Ellison et al. (2013), the Monte Carlo simulation smoothly treats non-relativistic to ultra-relativistic shocks. In Fig. 10 we show the profile of a trans-relativistic $\gamma_0 = 1.5$ shock for comparison with Fig. 5. Apart from γ_0, all input parameters are the same for the $\gamma_0 = 1.5$ and $\gamma_0 = 10$ cases. Since it is easier for accelerated particles to diffuse upstream against the inflowing plasma with $\gamma_0 = 1.5$ than against $\gamma_0 = 10$, the NL shock precursor is much more extended than it is for $\gamma_0 = 10$. The bulk flow speed, $u(x)$, is noticeably modified out to $x = L_{\rm UpS} = -300\, r_{\rm g0}$ (note the split log-linear x-axis in Fig. 10.).

As in the $\gamma_0 = 10$ case, the momentum and energy fluxes are not conserved in the UM shock but are within a few per cent of the far upstream values once the shock structure is modified by the CR backpressure. For $\gamma_0 = 1.5$, the overall compression ratio must

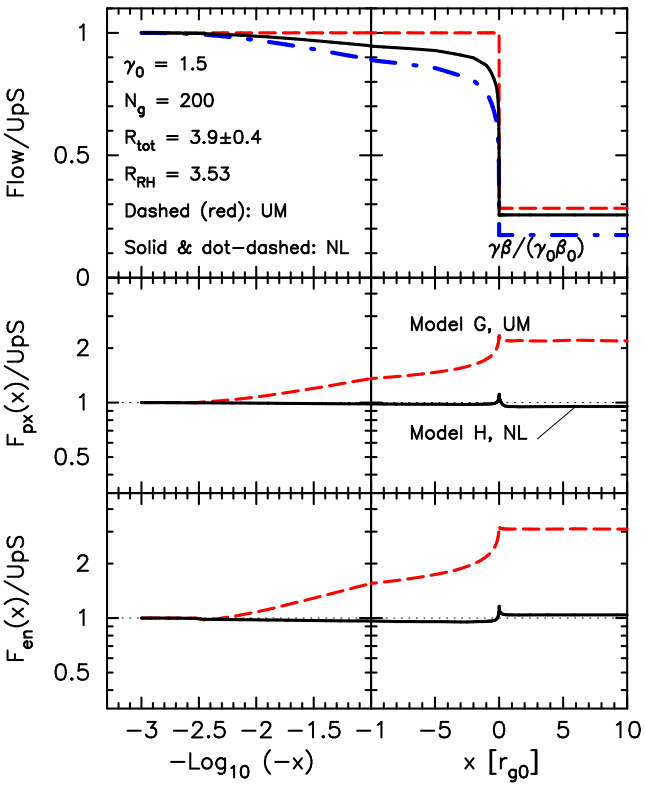

Figure 10. All curves are as in Fig. 5 for $\gamma_0 = 1.5$. The dashed (red) curves are the UM (Model G) case while the solid (black) and dot–dashed (blue) curves are the NL (Model H) profiles. The upstream and downstream FEBs are $L_{\rm UpS} = -300\, r_{\rm g0}$ and $L_{\rm DwS} = +1000\, r_{\rm g0}$, as in Fig. 5, but these distances differ in absolute units since u_0 varies between $\gamma_0 = 10$ and $\gamma_0 = 1.5$.

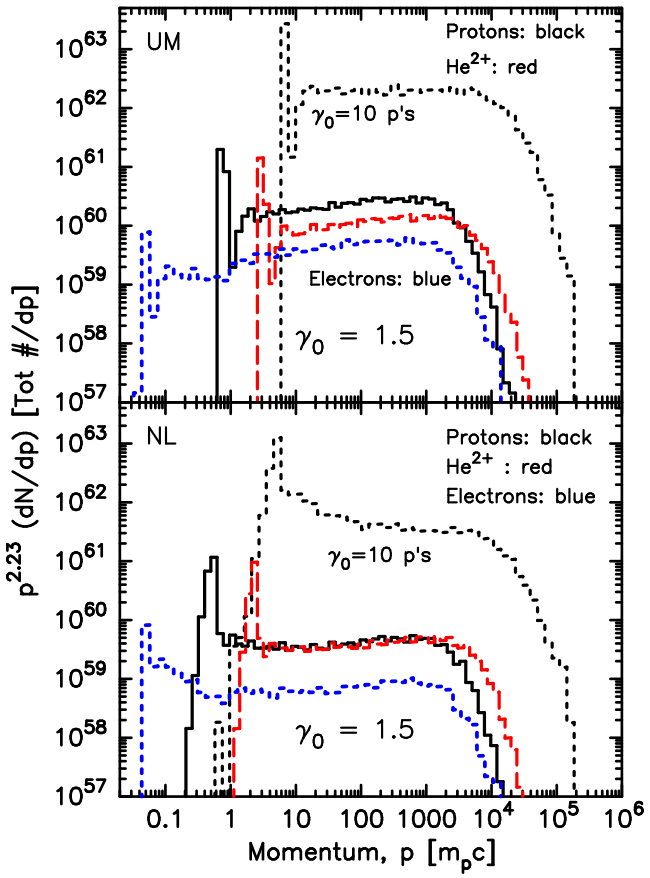

Figure 11. Except for the dotted (black) curves labelled '$\gamma_0 = 10$ p's' all spectra are downstream, LPF spectra for the unmodified $\gamma_0 = 1.5$ shock (top panel, Model G) and the non-linear $\gamma_0 = 1.5$ shock (bottom panel, Model H) shown in Fig. 10. The curves labelled '$\gamma_0 = 10$ p's' are identical to those in Fig. 6.

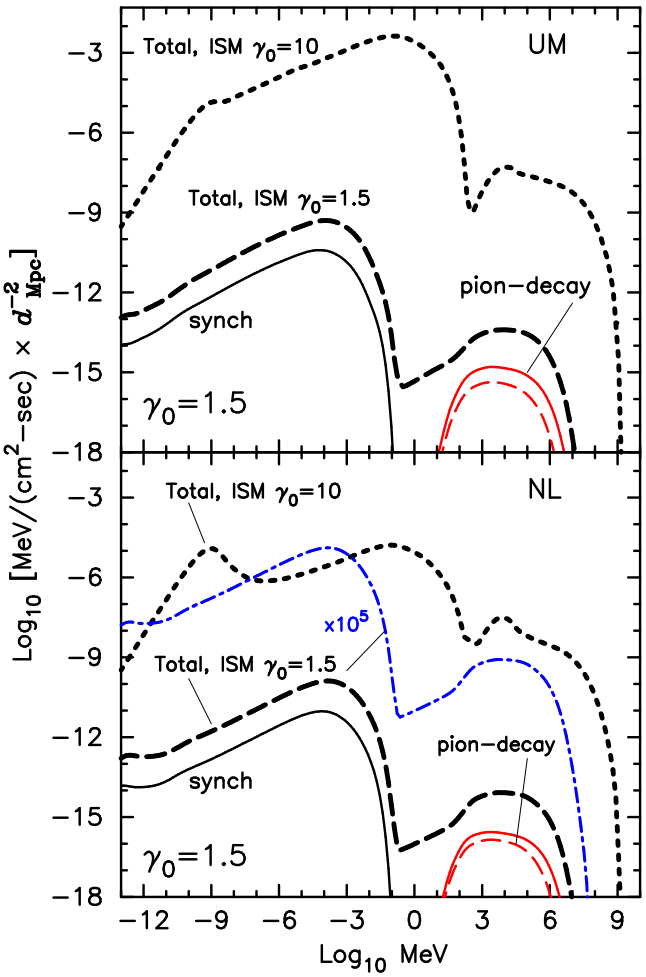

Figure 12. Photon emission for the UM (Model G) and NL (Model H) shocks shown in Figs 10 and 11. Except for the dotted (black) curves labelled 'Total, ISM $\gamma_0 = 10$', all curves are for the $\gamma_0 = 1.5$ shock and are in the same format as in Fig. 7. The dashed (black) curves are the total emission transformed to the ISM frame for an observer at $x = -d_{\rm Mpc}$ Mpc, at an angle within $1/\gamma_0$ from the shock normal. The dot–dashed (blue) curve in the lower panel is the total ISM frame $\gamma_0 = 1.5$ emission multiplied by 10^5.

also be increased to conserve momentum and energy and we find $R_{\rm tot} = 3.9 \pm 0.4$, where the uncertainty comes from statistics and errors inherent in the Monte Carlo smoothing algorithm. This result is similar to that given in Ellison et al. (2013) except here we have included He^{2+} and electrons in determining the self-consistent shock structure, and we use a downstream FEB as well as an upstream one.

In Fig. 11 we show the particle spectra for $\gamma_0 = 1.5$ in the same format as Fig. 6 except we have added the $\gamma_0 = 10$ proton spectra for comparison. The $\gamma_0 = 1.5$ spectra are harder than those for $\gamma_0 = 10$ mainly because $R_{\rm tot}$ is larger. A comparison of the e/p ratio at $\sim 300\, m_{\rm p}c$ for the NL models in Fig. 6 ($e/p \sim 1/300$) and Fig. 11 ($e/p \sim 1/6$) shows that the $\gamma_0 = 1.5$ shock is much more effective in injecting and accelerating electrons than the $\gamma_0 = 10$ shock. However, the maximum momentum is noticeably lower for $\gamma_0 = 1.5$ and the 'thermal' peak is also lower since, for downstream spectra, it occurs at $\sim \gamma_0 m_{\rm p}c$ for protons in the UM shock. The 'thermal' peak is at a noticeably lower momentum in the NL case.

Another important difference is the normalization. The $\gamma_0 = 10$ proton distributions are about a factor of 100 above the $\gamma_0 = 1.5$ spectra in the quasi-power law region. This comes about for two primary reasons. The $\gamma_0 = 10$ shock has a considerably higher downstream density since $n_2 = \gamma_0 \beta_0 n_0/(\gamma_2 \beta_2)$ and, with $r_{\rm g0}$ being larger, the number of particles in the distribution is larger. Another cause is that the spectra are multiplied by $p^{2.23}$ rather than by p. The area under a $\mathrm{d}N/\mathrm{d}\log(p)$ curve would be the total number of particles. But $\mathrm{d}N/\mathrm{d}\log(p) = p \cdot \mathrm{d}N/\mathrm{d}p$, so the extra 1.23 powers of p merely enhance the perceived importance of particles at higher momentum. Since the $\gamma_0 = 10$ shock contains particles at higher momenta, it also gets plotted higher on the $p^{2.23}\mathrm{d}N/\mathrm{d}p$ plot. The efficiencies for producing 100 MeV or greater energy particles are $\epsilon_{\rm H} = 0.52$, $\epsilon_{\rm He} = 0.27$, and $\epsilon_{\rm el} = 0.08$ for Model H; i.e. the $\gamma_0 = 1.5$ shock puts ~8 per cent of the shock energy into energetic electrons.

In Fig. 12 we show the photon emission for $\gamma_0 = 1.5$ in the same format as Fig. 7, with the addition of the total ISM frame emission for the $\gamma_0 = 10$ cases (dotted, black curves) added to the $\gamma_0 = 1.5$ cases (dashed, black curves) for comparison. The total emission for an observer at $D_{\rm obs} = -d_{\rm Mpc}$ Mpc is dramatically different for the two Lorentz factors. To highlight this in the lower panel, we have plotted the total ISM emission for $\gamma_0 = 1.5$ multiplied by 10^5 (dot–dashed, purple curve). The broad-band spectral shapes are very different between $\gamma_0 = 10$ and 1.5, and at ~1 keV the normalization differs by $\sim 10^5$.

Note that the NL $\gamma_0 = 1.5$ spectrum is harder than $\gamma_0 = 10$ in the GeV–TeV range but cuts off at a lower energy. The lower

cutoff energy shows up dramatically in the synchrotron emission. For $\gamma_0 = 1.5$ the synchrotron peak is around 1 keV, typical of SNR observations, while for $\gamma_0 = 10$, the peak is around 1 MeV. At radio emitting energies, the synchrotron spectra are very different because of the emission produced by the downstream thermal electrons. Of course we have not considered SSA here and this process will produce a low-energy cutoff in the synchrotron emission which may mask the emission from the thermal electrons. Since the frequencies of the thermal peak and SSA cutoff depend on B as $\nu_{\rm th} \propto B$ and $\nu_a \propto B^{1/5}$, respectively, a stronger magnetic field makes it more likely that the thermal peak will be resolved. We have also not considered γ-ray absorption between the GRB and Earth.

3.6 A/Z enhancement of heavy ions

The Monte Carlo code assumes that all scatterings are elastic in the LPF. This implies that an insignificant fraction of the particle energy is transferred to magnetic turbulence in the wave generation process. With elastic scattering, $\gamma_i v_i \propto p_i/A$ remains constant in a scattering event, where γ_i and v_i are local frame values. The energy gain particles receive on crossing the shock, which is determined by a Lorentz transformation between the two frames, also scales as p_i/A. In our plane-parallel approximation, the probability that particles make a set number of shock crossings also depends only on $\gamma_i v_i$. Thus an UM shock, with the Monte Carlo assumptions, will treat all particles identically in momentum per nucleon, including the thermal leakage injection.

An exception to this occurs if the acceleration is limited by a boundary at a fixed distance, as we assume here, or by a maximum acceleration time. Since we assume equation (2), diffusion length and acceleration time both scale as $(A/Z)(p_i/A)$ for $v_i \sim c$. Thus, apart from the normalization set by input parameters and the maximum momentum cutoff, all species should have identical spectra when plotted against p/A. With a fixed FEB, high A/Z particles will turn over at a lower p/A than low A/Z particles.

For Models I, D, and G in Fig. 13, we show downstream, shock frame, proton and He^{2+} spectra for UM shocks plotted in p/A units. Except for statistical variations, a factor of 10 normalization since $n_\alpha = 0.1 n_{\rm p}$, and the high momentum cutoff, the proton and He^{2+} spectra are identical. Electrons are not plotted but would show the same effect. In the corresponding NL Models J, E, and H, a clear enhancement of He^{2+}, produced solely because the shock structure in smoothed by the backpressure of accelerated particles, is seen. For the $\gamma_0 = 30$ Model J, $\epsilon_{\rm H} = 0.66$ and $\epsilon_{\rm He} = 0.34$.

The factor of 2 enhancement in the He^{2+}/p ratio seen in the NL models in Fig. 13 should be large enough to see clearly in PIC simulations. Since this enhancement is a prediction that stems directly from important assumptions of efficient *Fermi* acceleration and thermal leakage injection, adding helium to PIC simulations can test these assumptions. If the acceleration is efficient, and the A/Z effect is *not* seen, it implies that one or more of the following may be happening. (i) The accelerated protons and He^{2+} may be sharing significant energy with each other rather than interacting mainly elastically with the background turbulence. If this is the case, it will influence all aspects of *Fermi* acceleration. (ii) The particle mean free-path may not be a monotonically increasing function of momentum or it may differ substantially for protons and He^{2+}. (iii) Different A/Z particles may interact differently with the viscous subshock layer. A basic assumption for thermal leakage injection is that the subshock is essentially transparent, i.e. phenomena such as cross-shock potentials or large-scale turbulence do not strongly influence the injection process. If these phenomena are important, it is likely they will influence different A/Z particles differently, modifying the A/Z enhancement seen in Fig. 13.

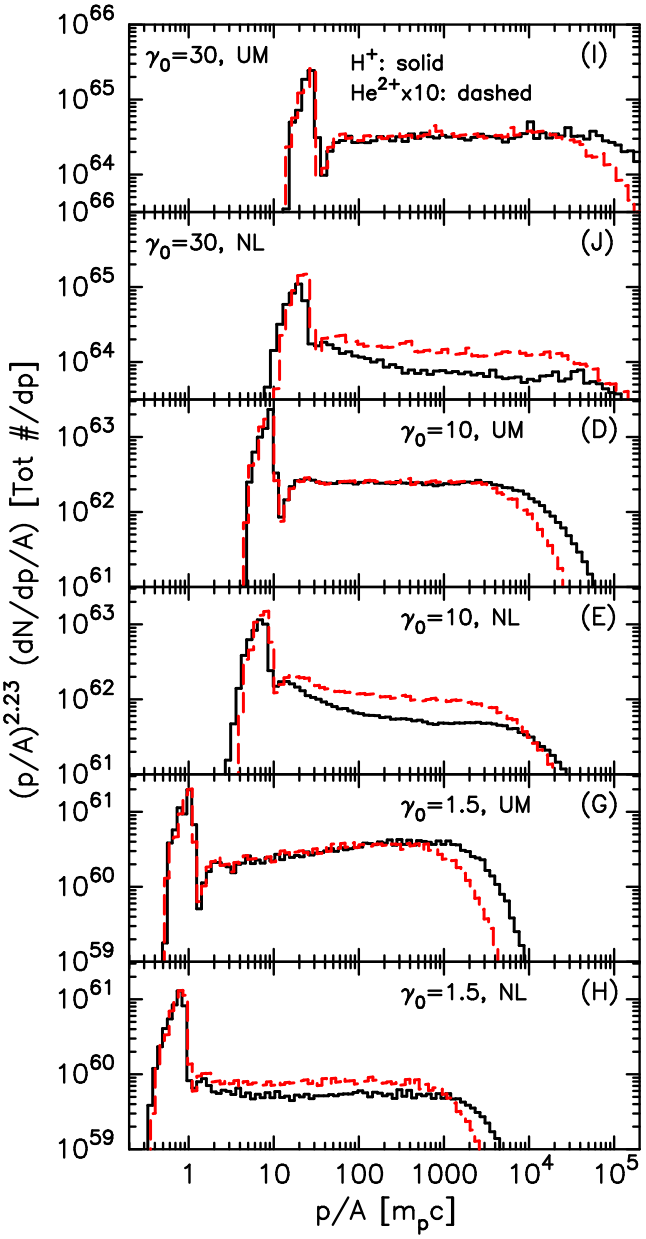

Figure 13. Models I, D, and G show proton and He^{2+} spectra for UM shocks, while Models J, E, and H are the corresponding spectra for the NL shocks. In all cases, the He^{2+} spectra are multiplied by 10 to adjust for the ambient number density. When plotted in p/A units the UM spectra are identical except for statistics and the maximum momentum cutoff. The NL shocks show a clear A/Z enhancement in the He^{2+}/p ratio.

4 CONCLUSIONS

As complicated as particle acceleration in relativistic shocks may be, one aspect is profoundly simple: if the acceleration is efficient and a sizable fraction of the bulk plasma flow energy is put into individual accelerated particles, as is often assumed in applications (e.g. Kulkarni et al. 1999; Piran et al. 2001; Piran 2004; Mészáros 2006), the accelerated particles must self-consistently modify the shock structure to conserve momentum and energy regardless of the

plasma physics details. Assuming first-order *Fermi* acceleration, we have investigated how the kinematics of shock modification influences the relative acceleration of electrons, protons, and heavy elements (i.e. He^{2+}) using a Monte Carlo simulation with a dynamic range large enough to model acceleration from injection at non-relativistic thermal energies to ultra-relativistic CR energies. Fig. 4 shows a 12 decade range in plasma-frame momentum and a greater than 20 decade range in dN/dp. A corresponding range in photon emission is also obtained (e.g. Fig. 12).

The underlying wave–particle plasma interactions, which are parametrized in the Monte Carlo code, will influence details of the shock modification and the resultant radiation; they will determine if acceleration is, in fact, efficient and set the maximum energy particles obtain. However, our results show general aspects that are largely independent of the poorly known plasma physics details if the acceleration is efficient. Considering only the kinematics, electrons will be accelerated much less efficiently than ions if the shock structure is modified by the heavy particles. This result assumes that the heavy particles and electrons diffuse in a similar fashion, as indicated in equation (1). If this is the case, the A/Z enhancement effect we describe increases the injection and acceleration efficiency of high A/Z particles compared to low A/Z ones. This dramatically decreases the abundance of accelerated electrons compared to heavier ions (e.g. Fig. 6). The kinematics suggest that relativistic shocks will not be able to place a sizable fraction of the shock kinetic energy flux into leptons if protons are present.

Of course, beyond kinematics, the magnetic turbulence produced by wave–particle interactions plays a critical role and recent results (e.g. Sironi & Spitkovsky 2011; Kumar et al. 2015) show that some fraction of the proton energy can be transferred to electrons in the shock precursor via magnetic turbulence. These PIC results are particularly important for astrophysical applications where the radiating electrons presumably contain a sizable fraction of the available energy budget. In relativistic shocks, heavy elements must transfer a sizable fraction of their energy to electrons for *Fermi* acceleration to be relevant for electrons.

We have modelled this energy transfer by including a parameter, $f_{\rm ion}$, that sets the fraction of ion energy transferred to electrons as the particles first cross the subshock. While the effect of $f_{\rm ion}$ is large (e.g. Fig. 3), kinematics must still play a role: light and heavy particles will be treated differently in relativistic flows. This is seen clearly in Figs 6 and 11 where, for a given $f_{\rm ion}$, the e/p ratio drops substantially between the UM case (where no A/Z effect occurs) and the NL case. Figs 6 and 11, where $f_{\rm ion} = 0.1$ for both the $\gamma_0 = 10$ and 1.5 shocks, also show that a larger fraction of ion energy must be transferred to electrons for high Lorentz factor shocks to produce a significant e/p ratio.

We make a clear prediction that is directly testable with PIC simulations. If *Fermi* acceleration is efficient enough so the shock structure is modified by the backpressure of accelerated particles, heavy element ions will show a clear enhancement over protons (i.e. Fig. 13). We know of no non-kinematic effects (e.g. cross-shock potentials, energy transfer via wave–particle interactions, or other electrostatic processes) that can produce such an enhancement.

The combined processes of energy transfer from heavy particles to electrons, and the kinematics of shock smoothing, produce strong signatures on the radiation emitted by these particles. In Fig. 12 we show results for $\gamma_0 = 10$ and $\gamma_0 = 1.5$. Since there are a number of important parameters that influence the emission, such as shock Lorentz factor, ambient density, magnetic field, and size of the emitting region, it is non-trivial to characterize the emission. Nevertheless, some general properties stem mainly from the kinematics and should hold regardless of the plasma physics details.

Particle spectra should harden as the shock speed decreases from fully relativistic to non-relativistic speeds, mainly because the shock compression ratio increases and, for low enough γ_0, $R_{\rm tot} > R_{\rm RH}$ (see fig. 10 in Ellison et al. 2013). However, even though the compression ratio (defined as $R_{\rm tot} = u_0/u_2$) is lower for ultra-relativistic shocks, the downstream local plasma number density $n_2 = \gamma_0\beta_0 n_0/(\gamma_2\beta_2)$ can be large, enhancing the pion-decay emission more than IC and synchrotron. The possibility of a significant change in the character of non-linear effects in the trans-relativistic regime, as well as the fact that trans-relativistic shocks have been observed (e.g. Soderberg et al. 2010), makes this an important area for future work.

The magnetic field is a critical parameter for synchrotron emission and, with the exception of Model C, we have assumed $B_0 = 100$ μG for the background field. In our plane-parallel approximation, the background field remains constant throughout the shock. Values of hundreds of μG can be expected for a shock moving through an ambient field of a few μG when compression and amplification are considered. Compression will increase the field by a factor $\sim\gamma_0$ and NL amplification, as believed to occur in strong, non-relativistic shocks in young SNRs (see, for example, Bell 2004; Vladimirov et al. 2009; Bykov et al. 2014, and references therein), may increase the strength further. For simplicity, we have not attempted to included compression or magnetic field amplification of the magnetic field here. Field compression is included in Warren (2015).

One important aspect of the changing afterglow emission as the shock slows from ultra-relativistic to non-relativistic speeds is the position of the synchrotron peak. As seen in Fig. 12, the peak shifts from ∼MeV to ∼keV as the shock slows from $\gamma_0 = 10$ to $\gamma_0 = 1.5$. A detailed evolutionary model of GRB afterglows using Monte Carlo techniques for NL *Fermi* acceleration is presented in Warren (2015). In this afterglow model, the Monte Carlo simulation is combined with an analytic or numerical description of the jet-shock evolution. The shock accelerated particles and resultant radiation are calculated at various times as the shock moves through the jet and the total emission observed at Earth is determined.

We caution that, for simplicity, we have assumed Bohm diffusion here (i.e. equation 2; $\lambda_{\rm mfp} = r_{\rm g} \propto p$) whereas the actual scattering process in relativistic plasmas is certain to be more complicated (e.g. Lemoine & Pelletier 2010). In particular, particles interacting with the small-scale turbulence generated by the Weibel instability are more likely to have $\lambda_{\rm mfp} \propto p^2$ and additional instabilities may contribute longer scale turbulence with a different momentum dependence (e.g. Casse et al. 2013; Lemoine et al. 2014). In fact, the momentum dependence and normalization of $\lambda_{\rm mfp}$ can be expected to vary with momentum as well as position relative to the subshock. While a first-principles determination of $\lambda_{\rm mfp}$ will undoubtedly require PIC simulations, the non-linear effects we describe here stem from basic considerations of momentum and energy conservation and should persist if first-order *Fermi* acceleration is efficient and $\lambda_{\rm mfp}$ is an increasing function of p. Bearing in mind our simple scattering assumptions, we believe this work is the first to include electrons, protons, and heavier elements in a non-linear relativistic shock acceleration model. We predict an A/Z enhancement effect for heavy ions in relativistic shock acceleration, and include the photon emission consistently with non-linear particle acceleration. Nevertheless, modifying the scattering prescription is certain to produce important quantitative differences, particularly for the photon emission which is strongly dependent on the maximum CR energy,

and we are generalizing the Monte Carlo technique to include more realistic forms for $\lambda_{\rm mfp}$ which will be presented in future work.

ACKNOWLEDGEMENTS

The authors acknowledge useful comments by an anonymous referee and wish to thank Hirotaka Ito, John Kirk, Davide Lazzati, Martin Lemoine, Guy Pelletier, Steve Reynolds, and Lorenzo Sironi for helpful discussions. DCE and DCW acknowledge support from NASA grant NNX11AE03G. AMB was partially supported by the RAS Presidium Programm and the RAS OFN Programm n15. S-HL acknowledges support from a JAXA International Top Young Fellowship. DCE and S-HL wish to thank the International Space Science Institute (ISSI) in Bern where part of this work was done.

REFERENCES

Achterberg A., Gallant Y. A., Kirk J. G., Guthmann A. W., 2001, MNRAS, 328, 393
Ackermann M. et al., 2013, ApJ, 763, 71
Baring M. G., Ogilvie K. W., Ellison D. C., Forsyth R. J., 1997, ApJ, 476, 889
Baring M. G., Ellison D. C., Reynolds S. P., Grenier I. A., Goret P., 1999, ApJ, 513, 311
Bednarz J., Ostrowski M., 1998, Phys. Rev. Lett., 80, 3911
Bell A. R., 2004, MNRAS, 353, 550
Berezhko E. G., Ellison D. C., 1999, ApJ, 526, 385
Binns W. R. et al., 2014, ApJ, 788, 18
Bykov A. M., Treumann R. A., 2011, A&AR, 19, 42
Bykov A., Gehrels N., Krawczynski H., Lemoine M., Pelletier G., Pohl M., 2012, Space Sci. Rev., 173, 309
Bykov A. M., Ellison D. C., Osipov S. M., Vladimirov A. E., 2014, ApJ, 789, 137
Casse F., Marcowith A., Keppens R., 2013, MNRAS, 433, 940
Chakraborti S., Ray A., Soderberg A. M., Loeb A., Chandra P., 2011, Nat. Commun., 2, 175
Double G. P., Baring M. G., Jones F. C., Ellison D. C., 2004, ApJ, 600, 485
Eichler D., 1984, ApJ, 277, 429
Ellison D. C., Double G. P., 2002, Astropart. Phys., 18, 213
Ellison D. C., Double G. P., 2004, Astropart. Phys., 22, 323
Ellison D. C., Eichler D., 1984, ApJ, 286, 691
Ellison D. C., Jones F. C., Eichler D., 1981, J. Geophys. Z. Geophys., 50, 110
Ellison D. C., Moebius E., Paschmann G., 1990, ApJ, 352, 376
Ellison D. C., Baring M. G., Jones F. C., 1996, ApJ, 473, 1029
Ellison D. C., Drury L. O., Meyer J., 1997, ApJ, 487, 197
Ellison D. C., Warren D. C., Bykov A. M., 2013, ApJ, 776, 46
Gedalin M., Balikhin M. A., Eichler D., 2008, Phys. Rev. E, 77, 026403
Haugbølle T., 2011, ApJ, 739, L42
Hoshino M., Arons J., Gallant Y. A., Langdon A. B., 1992, ApJ, 390, 454
Jokipii J. R., 1971, Rev. Geophys. Space Phys., 9, 27
Jones F. C., 1968, Phys. Rev., 167, 1159
Jones F. C., Ellison D. C., 1991, Space Sci. Rev., 58, 259
Kamae T., Karlsson N., Mizuno T., Abe T., Koi T., 2006, ApJ, 647, 692
Kamae T., Karlsson N., Mizuno T., Abe T., Koi T., 2007, ApJ, 662, 779
Kato T. N., 2007, ApJ, 668, 974
Kelner S. R., Aharonian F. A., Bugayov V. V., 2009, Phys. Rev. D, 79, 039901
Keshet U., Waxman E., 2005, Phys. Rev. Lett., 94, 111102
Keshet U., Katz B., Spitkovsky A., Waxman E., 2009, ApJ, 693, L127
Kirk J. G., Reville B., 2010, ApJ, 710, L16
Kirk J. G., Guthmann A. W., Gallant Y. A., Achterberg A., 2000, ApJ, 542, 235
Kulkarni S. R. et al., 1999, Nataure, 398, 389
Kumar P., Zhang B., 2015, Phys. Rep., 506, 1
Kumar R., Eichler D., Gedalin M., 2015, ApJ, 806, 165
Lemoine M., Pelletier G., 2003, ApJ, 589, L73
Lemoine M., Pelletier G., 2010, MNRAS, 402, 321
Lemoine M., Pelletier G., 2011, MNRAS, 417, 1148
Lemoine M., Pelletier G., Gremillet L., Plotnikov I., 2014, Europhys. Lett., 106, 55001
Levinson A., 1992, ApJ, 401, 73
McKinney J. C., Uzdensky D. A., 2012, MNRAS, 419, 573
Mészáros P., 2006, Rep. Progress Phys., 69, 2259
Meyer J. P., Ellison D. C., 1999, in Ramaty R., Vangioni-Flam E., Cassé M., Olive K., eds, ASP Conf. Ser. Vol. 171, LiBeB Cosmic Rays, and Related X- and Gamma-Rays. Astron. Soc. Pac., San Francisco, p. 187
Meyer J., Drury L. O., Ellison D. C., 1997, ApJ, 487, 182
Niemiec J., Ostrowski M., 2006, ApJ, 641, 984
Nishikawa K.-I., Hardee P. E., Hededal C. B., Fishman G. J., 2006, ApJ, 642, 1267
Nishikawa K.-I., Hededal C. B., Hardee P. E., Fishman G. J., Kouveliotou C., Mizuno Y., 2007, Ap&SS, 307, 319
Nishikawa K.-I. et al., 2011, Adv. Space Res., 47, 1434
Orlando S., Petruk O., Bocchino F., Miceli M., 2011, A&A, 526, A129
Piran T., 2004, Rev. Modern Phys., 76, 1143
Piran T., Kumar P., Panaitescu A., Piro L., 2001, ApJ, 560, L167
Plotnikov I., Pelletier G., Lemoine M., 2011, A&A, 532, A68
Plotnikov I., Pelletier G., Lemoine M., 2013, MNRAS, 430, 1280
Rauch B. F. et al., 2010, ApJ, 722, 970
Reville B., Bell A. R., 2014, MNRAS, 439, 2050
Rybicki G. B., Lightman A. P., 1979, Radiative Processes in Astrophysics. Wiley-Interscience, New York
Sagi E., Nakar E., 2012, ApJ, 749, 80
Schlickeiser R., 2015, preprint (arXiv:1503.04737)
Sironi L., Spitkovsky A., 2009, ApJ, 698, 1523
Sironi L., Spitkovsky A., 2011, ApJ, 726, 75
Sironi L., Spitkovsky A., Arons J., 2013, ApJ, 771, 54
Sironi L., Petropoulou M., Giannios D., 2015, MNRAS, 450, 183
Soderberg A. M. et al., 2010, Nataure, 463, 513
Stockem A., Fiúza F., Fonseca R. A., Silva L. O., 2012, ApJ, 755, 68
Summerlin E. J., Baring M. G., 2012, ApJ, 745, 63
Vladimirov A. E., Bykov A. M., Ellison D. C., 2008, ApJ, 688, 1084
Vladimirov A. E., Bykov A. M., Ellison D. C., 2009, ApJ, 703, L29
Warren D. C., 2015, PhD thesis, North Carolina State University

This paper has been typeset from a TEX/LATEX file prepared by the author.